Astronomy & Astrophysics manuscript no. paper ©ESO 2014
March 19, 2014

A simulation of a flux rope ejection as seen by AIA

P.Pagano[1], D.H. Mackay[1], and S.Poedts[2]

[1] School of Mathematics and Statistics, University of St Andrews, North Haugh, St Andrews, Fife, Scotland KY16 9SS, UK.

[2] Dept. of Mathematics, Centre for Mathematical Plasma Astrophysics, KU Leuven, Celestijnenlaan 200B, 3001 Leuven, Belgium.

ABSTRACT

Context. Coronal mass ejections (CMEs) are the most violent phenomena observed on the Sun. Currently, Extreme Ultra Violet (EUV) images from the Atmospheric Imaging Assembly (AIA) on board the Solar Dynamic Observatory (SDO) are providing new insights on the early phase of CME evolution. In particular, it is now possible to obtain detailed observations on the ejection of magnetic flux ropes from the solar corona and how they become CMEs. While this is the case, these observations are complex to interpret in terms of basic physical mechanisms and quantities. To fully understand CMEs we need to compare equivalent quantities derived from both observations and theoretical models. This will aid us to validate the models and to bridge the gap between the models and observations.

Aims. In order to bridge the gap between models and EUV observations we aim to produce synthetized AIA observation from simluation of a flux rope ejection. Moreover, we intend to include the role of thermal conduction and radiative losses effects which are important for determining the temperature distribution of the solar corona during a CME.

Methods. We perform a simulation where a flux rope is ejected from the solar corona. From the density and temperature of the plasma in the simulation we synthesise AIA observations. The emission is then integrated along the line of sight using the instrumental response function of AIA.

Results. We sythesise observations of AIA in the channels at 304Å, 171Å, 335Å, and 94Å. The synthsized observations show a number of features similar to actual observations and in particular reproduce the general development of CMEs in the low corona as observed by AIA. In particular we find the erupting and expanding arcade in 304Å and 171Å channels and we observe the high temperature plasma in 335Å and 94Å channels.

Conclusions. The flux rope ejection produces many of the features found in AIA observations. This work, is therefore a step forward in bridging the gap between models and observations, and can lead to interesting interpretations of EUV observations in terms of flux rope ejections. We plan to improve the model in future studies in order to perform a more quantitative comparison.

Key words. MHD – Solar Corona – CME

1. Introduction

Coronal Mass Ejections (CMEs) are violent eruptions of plasma and magnetic flux from the solar corona. They have been observed since 1971 (Tousey 1973) with increasingly more accurate and precise instruments. While the majority of satellites built to study the Sun are also devoted to study CMEs, many aspects of CMEs remain an enigma, with outstanding questions being actively investigated by the solar community. One of the most recent satellites to study CMEs is the Solar Dynamic Observatory (SDO). In particular the Atmospheric Imaging Assembly instrument (AIA; (Lemen et al. 2012)) continuously observes the full solar disk providing observations in extreme ultraviolet (EUV) channels. Images from AIA enable us to observe with high spatial and temporal resolution the early phase of ejections and the regions from where they originate. Due to this, the underlying physics of the generator and propagation of CMEs can be studied. To date, solar observations stimulate many questions that theoretical models are not able to answer. To bridge the gap between models and observations, a key issue is to determine which features our models are already able to describe and what remains to be understood. This can only be carried out if equivalent quantities from theoretical models and observations can be compared.

Many models have been put forward to explain CMEs. One such model is the flux rope ejection model, where a magnetic flux rope is formed in the corona and is subsequently violently ejected (Forbes & Isenberg (1991), Amari et al. (2000), Fan & Gibson (2007)). Whether the flux rope ejection model can explain all CMEs or only some of them is still an open question, but direct observations have clearly linked the ejection of a flux rope with at least 40% of CMEs. For the remaining CMEs we do not have sufficient information to determine if a flux rope is present or not (Vourlidas et al. 2013). Only in a small percentage of cases we can exclude the presence of a flux rope. Moreover, additional studies, directly involving AIA, have shown that flux ropes are formed and ejected during a CME (Chen (2011) and Li & Zhang (2013)). From the theoretical point of view, a number of studies have shown that the ejection of a flux rope is sufficient to reproduce the main observed features of CMEs: Török & Kliem (2007), Fan (2010) and Aulanier et al. (2010) explain the ejection with the occurrence of a Torus instability; Fan (2009) and Archontis et al. (2009) with a flux emergence event; Savcheva et al. (2012) with the rotation of footpoints; Amari et al. (2003) with shearing and flux cancellation, while Amari et al. (2011) use convergence of foot points; finally Roussev et al. (2012) consider a global reorganization of the solar corona. Zuccarello et al. (2012) used STEREO observations to make a 3D reconstruction of the early evolution path of a CME and compared it to numerical simulations in order to determine the role of streamers in the deflection of CMEs towards the equatorial plane. Additionally, Pagano et al. (2013a) and Pagano et al. (2013b) have developed an approach where the flux rope ejection is modelled with MHD simulations. They start from an already out of equilibrium initial condition. In this scenario,

the flux rope formation generates the Lorentz force excess for the ejection. A technical innovation of this approach is that the flux rope formation is described by the Global Non Linear Force Free Field (GNLFFF) model (Mackay & van Ballegooijen 2006) and the final state of the GNLFFF is coupled with the initial condition of the MHD simulation. We base a significant part of the present work on these two papers and the approach developed within them.

The aim of this paper is to generate a technique that will enable us to directly compare the flux rope ejection model of Pagano et al. (2013b) with actual observations, in particular EUV emission seen by AIA. Our goal is to develop a tool to check the validity of our model and understand what needs to be improved to accurately describe solar eruptions. The strategy we follow is to reproduce AIA observations from a MHD simulation and then analyse these synthesized observations in order to determine differences and similarities with the actual observations. In order to pursue our strategy we perform a MHD simulation with an initial condition based on the parameter study carried out in Pagano et al. (2013b) where a flux rope is violently ejected. We also tune the thermodynamic parameters of the simulation in order to have a non isothermal initial profile. The flux rope has realistic values of density and temperature required for comparison with observations where it is represented by a denser and colder structure compared to its surroundings. During the evolution of the flux rope we compute the EUV emission from each plasma element of the MHD simulation. The emission is then integrated along the line of sight taking into account the instrumental response of each AIA channel. In this way we reproduce synthetic AIA images from our MHD model that can be analysed and compared with actual observations. Our strategy has already been applied by other authors. Pagano et al. (2008) reproduced UVCS/SoHo observations to study the passage of shocks connected to CMEs in the solar corona, Hoilijoki et al. (2013) calculated the resulting emission measure from a MHD simulation to study the propagation of MHD waves and Roussev et al. (2012) reproduced the soft X-ray emission from their simulation. Downs et al. (2011) in a global context reproduced EUV images from a CME simulation, and Lugaz et al. (2011) reproduced an observed flux rope ejection and synthetized the corresponding EIT images.

Another aim of this work is to assess the importance of the effects of thermal conduction and radiative losses when modelling a CME. Some previous work has already made important steps towards a realistic physical modelling of the solar corona, For example, Mok et al. (2005) studied the detailed thermal structure of an active region including the transition region, and Lionello et al. (2009) simulated the global corona over a period of several weeks including non-ideal MHD effects. Through this the authors developed an online tool to perform physically realistic EUV synthesis of a corona in near-equilibrium.

The present paper intends to put forward a simple but useful technique to study flux rope ejections. From this the long term goal is to make possible the comparison of equivalent quantities found in both EUV observations and EUV synthesized images. Of course, in order to significantly expand our knowledge of CMEs, in the near future we must go beyond the results of the present paper. We set out ambitious goals for future research, such as the study of specific CME events,

or the focus on individual structures observed during flux rope ejections (e.g. current sheets or shocks).

The paper is structured as follows: in Sec.2 we describe how the MHD simulation is set up and the evolution of the simulation. In Sec.3 we describe our technique used to reproduce AIA observations from the MHD simulation, in Sec.4 we show the results of our synthesized observations and the features they produce. Finally, in Sec.5 we discuss some aspects of the present work and in Sec.6 we draw some general conclusions.

2. MHD Simulation

In order to reproduce the EUV emission of the coronal plasma during a flux rope ejection, we first perform a MHD simulation where a flux rope ejection occurs. Subsequently, from the MHD simulation which provides the plasma density and temperature, as a function of time and position, we can infer the emission observable by AIA. We use the AMRVAC code developed at the KU Leuven to run the simulations (Keppens et al. 2012) to solve the MHD equations where gravity, thermal conduction and radiative losses are included as source terms

$$\frac{\partial \rho}{\partial t} = -\nabla \cdot (\rho \mathbf{v}), \tag{1}$$

$$\frac{\partial \rho \mathbf{v}}{\partial t} + \nabla \cdot (\rho \mathbf{v}\mathbf{v}) = -\nabla p + \frac{(\nabla \times \mathbf{B}) \times \mathbf{B})}{4\pi} + \rho \mathbf{g}, \tag{2}$$

$$\frac{\partial \mathbf{B}}{\partial t} = \nabla \times (\mathbf{v} \times \mathbf{B}), \tag{3}$$

$$\frac{\partial e}{\partial t} + \nabla \cdot [(e + p)\mathbf{v}] = \rho \mathbf{g} \cdot \mathbf{v} - n^2 \chi(T) - \nabla \cdot \mathbf{F_c}, \tag{4}$$

where t is the time, ρ is density, $\mathbf{v}$ velocity, p thermal pressure, $\mathbf{B}$ magnetic field, e the total energy, n number density, $\mathbf{F_c}$ the conductive flux according to Spitzer (1962), and $\chi(T)$ the radiative losses per unit emission measure (Colgan et al. 2008). To close the set of Eq.1-4 we have a relation between internal, total, kinetic and magnetic energy

$$\frac{p}{\gamma - 1} = e - \frac{1}{2}\rho \mathbf{v}^2 - \frac{\mathbf{B}^2}{8\pi} \tag{5}$$

where $\gamma = 5/3$ denotes the ratio of specific heats and the expression for solar gravitational acceleration

$$\mathbf{g} = -\frac{GM_\odot}{r^2}\hat{r}, \tag{6}$$

where G is the Gravitational constant and $M_\odot$ denotes the mass of the Sun, r is the radial distance from the centre of the Sun, and $\hat{r}$ is the corresponding unit vector. In order to gain accuracy in the description of the thermal pressure, we make use of the magnetic field splitting technique (Powell et al. 1999), as explained in detail in Sec.2.3 of Pagano et al. (2013a).

We start from the results of Pagano et al. (2013a) and Pagano et al. (2013b) to set up the MHD simulation. In particular, we adopt the same magnetic configuration that leads to flux rope ejections in these studies. The configuration of the magnetic field is taken from Day 19 in the simulation of Mackay & van Ballegooijen (2006). Pagano et al. (2013a) in Sec.2.2 explain in detail how the magnetic field distribution is imported from the GNLFFF model of Mackay & van Ballegooijen (2006) to our MHD simulations. In the present paper the simulation domain extends over 3 $R_\odot$ in the radial dimension starting from $r = R_\odot$. The colatitude, θ, spans from $\theta = 30°$ to $\theta = 100°$ and the longitude, ϕ, spans over 90°. This domain extends to a larger radial distance than the domain used in Mackay & van Ballegooijen (2006) from which we import the magnetic configuration. To define the magnetic field for $r > 2.5\,R_\odot$, we assume it to be purely radial ($B_\theta = B_\phi = 0$) where the magnetic flux is assumed to be conserved

$$B_r(r > 2.5R_\odot, \theta, \phi) = B_r(2.5R_\odot, \theta, \phi)\frac{2.5^2}{r^2}. \quad (7)$$

Fig.1 shows a 3D plot of the initial magnetic configuration. The flux rope (red lines) lies in the θ direction. The flux rope is close to the point where an eruption will occur as it can no longer be held down by the overlying arcades. The arcades are shown by the blue lines above which lies the external magnetic field lines (green lines). Some of the external magnetic field lines belong to the external arcade while some are open.

The boundary conditions of the MHD simulation are treated with a system of ghost cells. Open boundary conditions are imposed at the outer boundary, reflective boundary conditions are set at the θ boundaries and the ϕ boundaries are periodic. The θ boundary condition is designed to not allow any plasma or magnetic flux through, while the ϕ boundary condition allows the plasma and magnetic field to freely evolve across the boundaries. These boundary conditions match those used in Mackay & van Ballegooijen (2006). In our simulations the expanding and propagating flux rope only interacts with the θ and ϕ boundaries near the end of the simulations, thus they do not affect our main results regarding the initiation and propagation of the CME. At the lower boundary we impose a fixed boundary condition taken from the first four θ-ϕ planes of cells derived from the GNLFFF model. The computational domain is composed of $256 \times 128 \times 128$ cells distributed in a uniform grid.

In Pagano et al. (2013a) the production of the initial condition from the GNLFFF simulation and the dynamics of the ejection are discussed in detail, while Pagano et al. (2013b) identified the parameter space where the flux rope is fully ejected. In the present work the simulation parameters are fixed to generate a CME. In particular, Pagano et al. (2013b) have shown that having a low-β region above the flux rope is a critical factor for the occurrence of the flux rope ejection.

As our aim is to reproduce satellite observations, we set up a simulation with realistic values for plasma density and temperature. In order to do so, we prescribe a non isothermal solar corona.

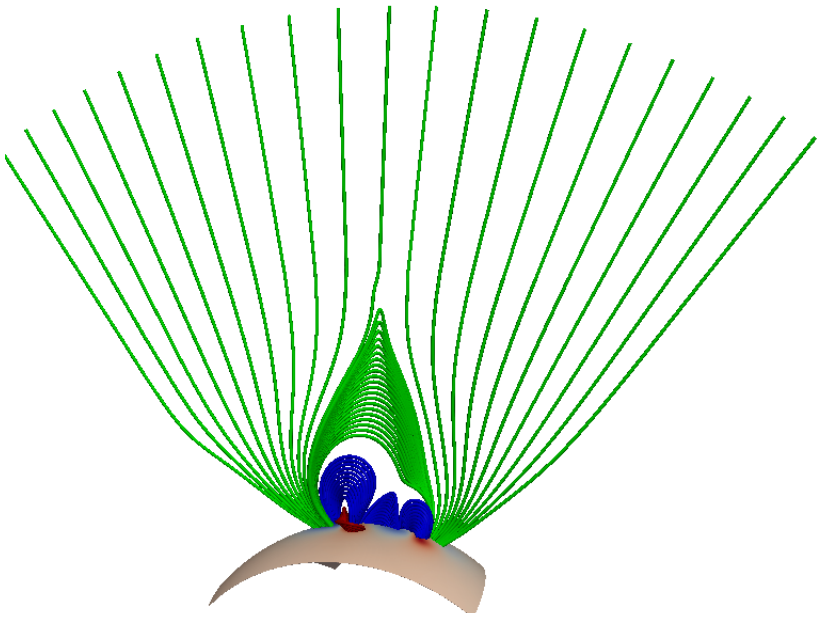

Fig. 1. Magnetic field configuration used as the initial condition in all the MHD simulations. Red lines represent the flux rope, blue lines the arcades, green lines the external magnetic field. The lower boundary is coloured according to the polarity of the magnetic field from blue (negative) to red (positive) in arbitrary units.

To specify the temperature distribution we use the function $T(\mathbf{B})$:

$$T(\mathbf{B}) = [(\frac{6}{2 + (B_\theta/|B|)} - 2)(T_{out} - T_{min}) + T_{min}](1 - G(\mathbf{B})) + T_{out}G(\mathbf{B}) \quad (8)$$

where T_{out} is the value of $T(\mathbf{B})$ where $B_\theta = 0$ and $G(\mathbf{B}) = 0$, while T_{min} determines the minimum allowed value for $T(\mathbf{B})$ where $B_\theta = |B|$ and $G(\mathbf{B}) = 0$. The function $G(\mathbf{B})$ is useful to bound the dependence of T on $\mathbf{B}$ to the regions where the magnetic field strength is significant. The form applied in the present paper is

$$G(\mathbf{B}) = e^{-\frac{|B|^2}{2B_*}} \quad (9)$$

where $B_* = 3\ G$ in our simulation. The choice of this ad hoc analytic formula is justified by the fact that in our set up the flux rope lies in the θ direction, with a positive B_θ. It is the only structure with a strong shear in the initial condition of our simulation. This allows us to produce a cool dense region at the location of the flux rope (i.e. high B_θ). In principle, it is possible to generalize this temperature distribution by replacing the θ direction with the direction of the flux rope axis. However for the present simulations this would have little effect.

The thermal pressure distribution is specified using the solution for hydrostatic equilibrium with uniform temperature set equal to T_{out}

$$p = \frac{\rho_{LB}}{\mu m_p} k_b 2T_{out} e^{-\frac{M_\odot G \mu m_p}{2T_{out}k_b R_\odot}} e^{\frac{M_\odot G \mu m_p}{2T_{out}k_b r}}, \quad (10)$$

where ρ_{LB} is the density at $r = R_\odot$ when $|B| = 0$, $\mu = 1.31$ is the average particle mass in the solar corona, m_p is the proton mass, k_b is Boltzmann constant. Finally, the density is simply given by the equation of state applied to Eq.8 and Eq.10:

$$\rho = \frac{p}{T(\mathbf{B})} \frac{\mu m_p}{k_b} \tag{11}$$

In our simulation we choose $T_{out} = 2\ MK$, $T_{min} = 10^4\ K$, $\rho_{LB} = 3.5 \times 10^{-15}\ g/cm^3$. With these values, we obtain the atmospheric profile shown in Fig.2 which shows a radial cut of density, thermal pressure, and temperature (solid lines) from the lower boundary to the external boundary passing through the centre of the LHS bipole (where the flux rope lies) and a cut of temperature along the center of the flux ropes at the lower boundary. In each graph for comparison the corresponding hydrostatic solution at $T = 2\ MK$ is shown (dashed line). The density profile (Fig.2a) shows how the coronal density decreases due to gravitational stratification. Below $r \sim 1.3\ R_\odot$ there is an excess of density with respect to the hydrostatic profile. This is due to the presence of the flux rope above the LHS bipole that is denser and cooler than the surroundings, as prescribed by our atmosphere model. The temperature profile (Fig.2b) shows a varying temperature structure. The flux rope at $T \sim 10^4\ K$ is cooler than the surroundings, while the external corona above the flux rope lies at $T = 2\ MK$. Similarly, the lower boundary of the simulation is mostly at $T = 2\ MK$ except for the locations around the PIL of the bipoles where the temperature is lower (Fig.2c). The LHS bipole shows a much lower temperatature than the RHS bipole, as on the LHS bipole there is a fully formed flux rope, which has a more prominent axial field component, B_θ. The thermal pressure profile (Fig.2d) is built to correspond to the hydrostatic profile.

It should be noted that Eq.8-11 do not produce a hydrostatic equilibrium because of the varying temperature dependence on B_θ. In contrast the thermal pressure profile assumes a constant temperature at $T = T_{out}$. Such an atmosphere if left to evolve would locally expand or contract depending on whether the temperature is larger or smaller than T_{out}. However, this has little or no effect on our simulation, as the dynamics is entirely governed by the out of equilibrium magnetic field configuration. This configuration immediately leads to the ejection of the flux rope which results in a major perturbation of the whole coronal environment before any significant motion due to gravity or thermal pressure gradients occurs. We note that the use of this atmosphere which is not in hydrostatic equilibrium is necessary to produce the ρ and T distributions required for realistic emission images.

In conclusion, our atmosphere is suitable to realistically describe the region surrounding a flux rope. While this is the case the values of density and thermal pressure appear too high for an in equilibrium outer solar corona. This is partly due to the fact that we do not consider a solar wind that would significantly change the outer coronal values of density and thermal pressure. However, the plasma properties in the external corona are not important for the present study which considers the violent flux rope propagation and expansion in the low corona.

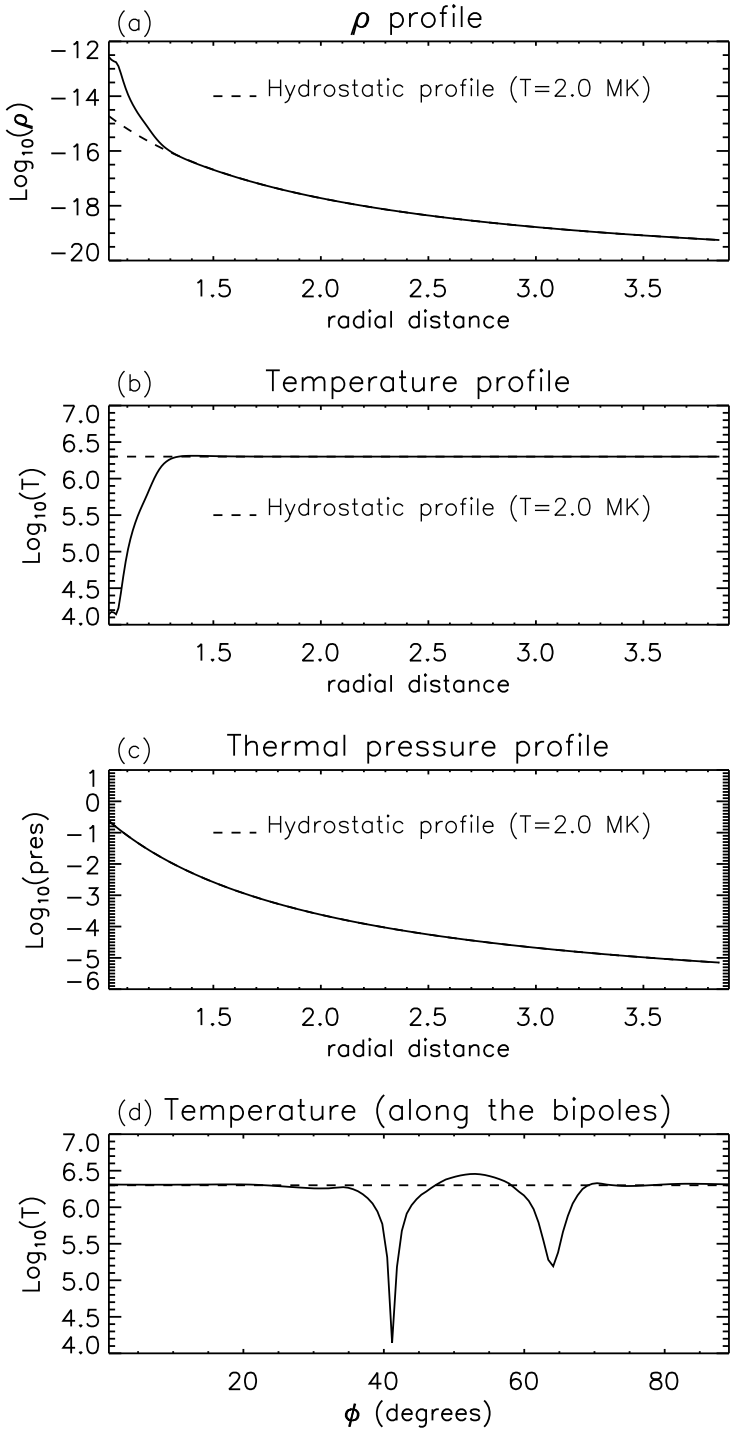

Fig. 2. Profiles along the radial direction above the center of the LHS bipole at $t = 0$ *min* of (a) $Log_{10}(\rho)$, (b) $Log_{10}(T)$, (c) $Log_{10}(p)$. (d) Profile along the ϕ direction along the center of the bipoles of $Log_{10}(T)$. The dashed lines show the equivalent profiles for a coronal atmosphere in hydrostatic equilibrium at $T = 2$ *MK*.

2.1. Evolution of the MHD simulation

The MHD simulation shows a very similar evolution to those already analysed in Pagano et al. (2013b). The evolution is illustrated in Fig.3 where maps of density and temperature are shown in the $(r - \phi)$ plane passing through the centre of the bipoles. Initially the flux rope lies near the lower boundary and as soon as the system is allowed to evolve it is ejected upwards. Once the ejection

occurs the high density region rises. Initially the high density region remains in the shape of the ejected flux rope (Fig.3b), however near the end of the simulation it is less identifiable with the flux rope (Fig.3c). After approximately 30 minutes the front of the high density front reaches the outer boundary at 4 $R_\odot$.

The magnetic field configuration undergoes a major evolution and reconfiguration as a result of the ejection. While this occurs, the flux rope can still be identified during the entire simulation by the presence of a strong axial component of the magnetic field (B_θ - not shown, see Pagano et al. (2013b), Sec.3.1). The magnetic flux is expelled outwards and at $t = 23.20min$ (Fig.3c) a region of compressed magnetic field is visible ahead of the ejection, where the front of the ejection compresses both plasma and magnetic flux.

The flux rope is initially colder than the surrounding corona at approximately $T = 10^4\ K$. At the initial stage of the ejection its temperature increases and a region of temperature about $T = 1\ MK$ is produced. This region then expands and propagates upwards and the density starts decreasing along with the temperature. At the same time a hot front heated by compression propagates ahead of the flux rope, where the temperature is about $10^7\ K$, but the temperarture distribution is very disuniform (Fig.3e). This front clearly marks where the perturbation of the ejection has reached (Fig.3f).

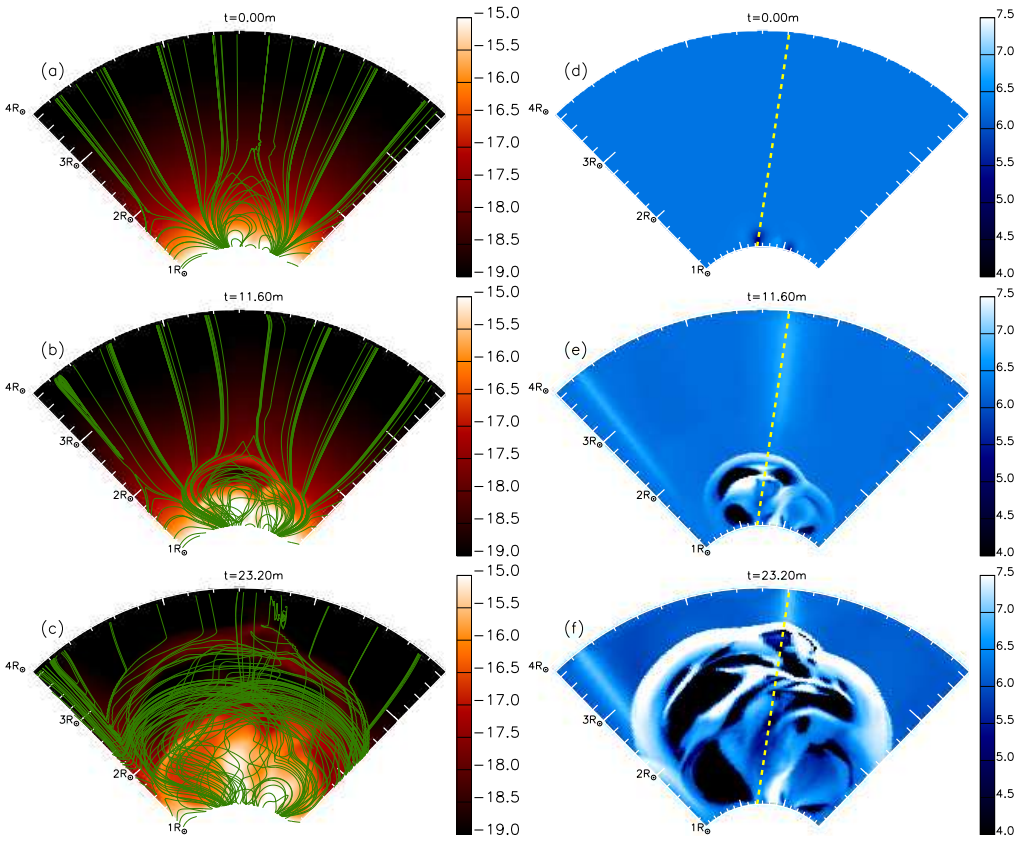

Fig. 3. (a)-(c) Maps of $Log_{10}(\rho)$ in the $(r - \phi)$ plane passing through the centre of the bipoles at $t = 0$, $t = 11.60$ and $t = 23.20min$. Superimposed are magnetic field lines plotted from the same starting points (green lines). (d)-(f) Maps of $Log_{10}(T)$ on the same plane and at the same times. Maps show the full domain of our simulations from $r = 1\ R_\odot$ to $r = 4\ R_\odot$. The yellow dashed line is the cut for the plots in Fig.2 and Fig.4. The temporal evolution is available in the on-line edition.

As explained in Pagano et al. (2013a), the flux rope is initially ejected radially outwards because of an excess of the radial Lorentz force underneath. However, immediately afterwards, the ejection propagates non-radially in the direction of the null point which lies above the arcade system (yellow dashed line in Fig.3d-f). This is due to the fact that the confining Lorentz force exterted by the magnetic arcades is weaker there and thus this becomes a favourale escape direction for the flux rope. This is particularly visible in Fig.3d-f, where the colder plasma moves along the yellow dashed line.

In order to accurately follow the density and temperature evolution, we show in Fig.4 the profile of density and temperature above the centre of the LHS bipole along the direction of ejection (yellow cut in Fig.3d) at $t = 0$, 11.60 and 23.20 *min*. At each time, the position of the centre of the flux rope is shown with a dashed vertical line. The centre of the flux rope is located where the quantity $B_\theta/|B|$ is maximum along the considered cut. In our framework, this identifies where the strongest axial component of the flux rope lies.

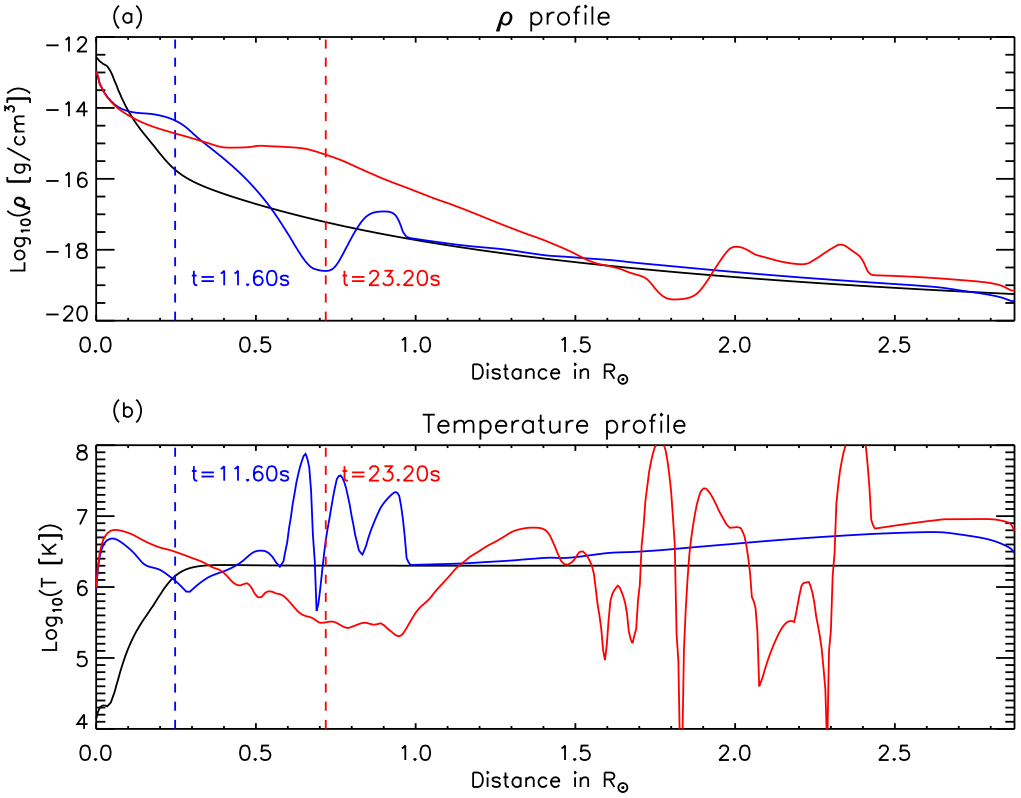

Fig. 4. (a) Profiles of $Log_{10}(\rho)$. (b) Profiles of $Log_{10}(T)$. All the profiles are along the yellow dashed line in Fig.3d which represents the direction of the flux rope ejection at $t = 0$ *min* (black line), $t = 11.60$ *min* (blue line) and $t = 23.20$ *min* (red line). The dashed lines mark the position of the center of the flux rope at each time.

At all times, the flux rope lies where an excess in density is present (Fig.4a). The extension of the excess density region is the smallest at $t = 0min$, and it expands with time. At $t = 11.60min$ the flux rope extends over 0.5 $R_\odot$. Simultaneously, the flux rope density decreases from $\rho \sim 10^{-12.5}$ g/cm^3 to $\rho \sim 10^{-15}$ g/cm^3. A dense front is located ahead of the propagating flux rope at larger radial distance. This front does not exist at $t = 0min$ as it is a consequence of the flux rope

propagation that compresses the plasma ahead of it. Through the simulation the density of the front is around $\rho \sim 10^{-17}\ g/cm^3$.

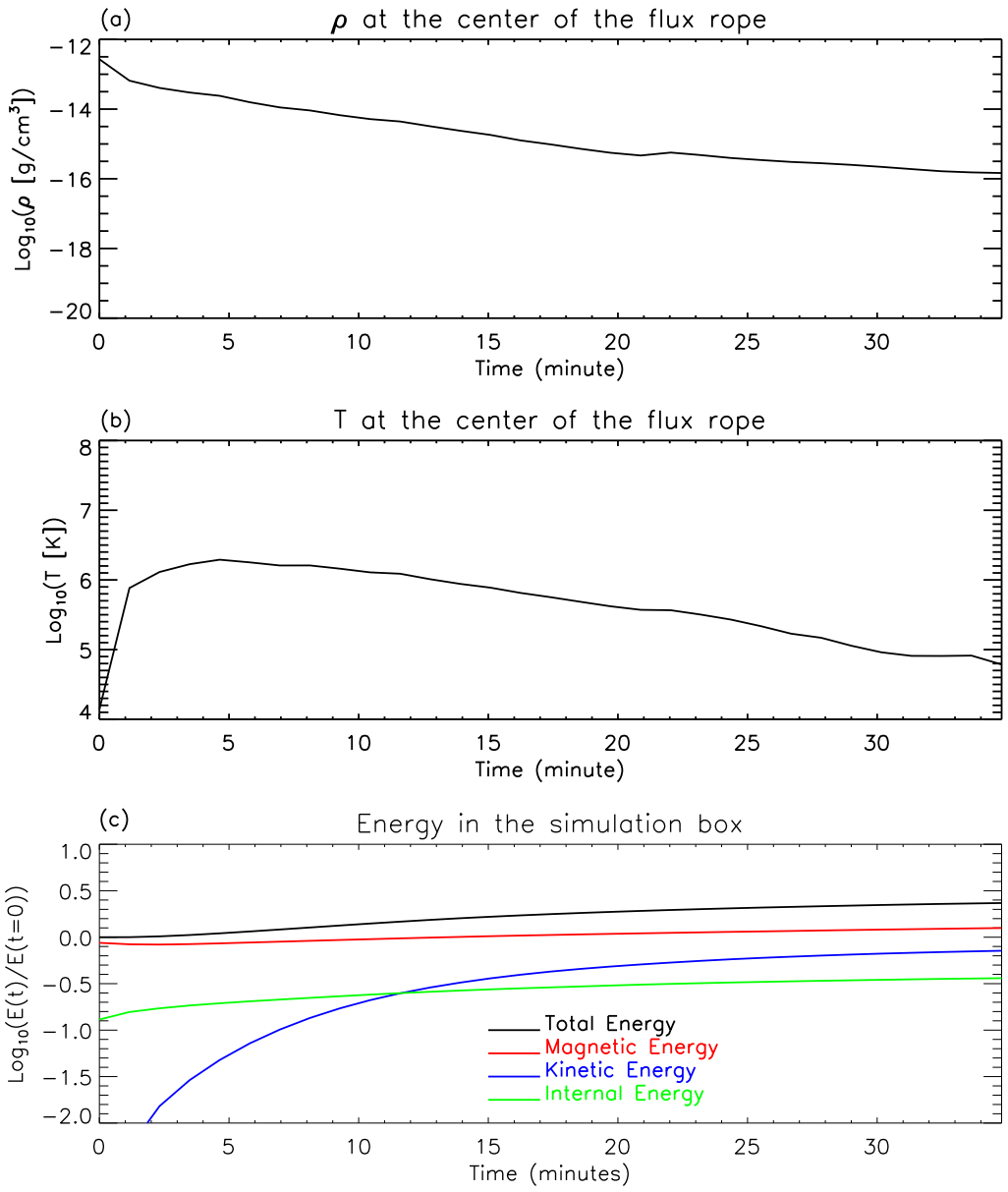

Fig. 5. (a) Value of $Log_{10}(\rho)$ at the center of the flux rope as a function of time. (b) Value of $Log_{10}(T)$ at the center of the flux rope as a function of time. (c) Variation of each energy term in different colors integrated in the whole domain as function on time in units of the initial total energy.

Fig.4b shows the evolution of temperature along the same cut, where the flux rope is initially at $T = 10^4\ K$ and is colder than the surroundings. At $t = 11.60min$ the flux rope has been heated up to $T \sim 10^6\ K$ because of the conversion of magnetic energy into internal energy as a result of numerical diffusion. While it is initially heated, the temperature decreases to $T \sim 10^{5.5}\ K$ at $t = 23.20min$. It should be noted that at any time the position of the centre of the flux rope roughly correspons to a dip in temperature. The high density front seen in Fig.4a presents a very sharp gradient in temperature, as the compression occurring there heats the plasma beyond $T \sim 10^7\ K$, while the plasma ahead of the front is colder. The plasma ahead of the front in Fig.4b is heated by

the conversion of magnetic energy into thermal energy, as the considered cut is along a separatrix surface as shown also in Fig.3e-f.

Using the density and temperature at the centre of the flux rope we may follow the thermodynamic evolution of the flux rope. Fig.5a shows the evolution of the density at the centre of the flux rope as a function of time. The density steadly decreases from $\rho \sim 10^{-12}\ g/cm^3$ to $\rho \sim 10^{-16}\ g/cm^3$ because of the expansion. The temperature (Fig.5b) initially increases rapidly by two orders of magnitude in less than 5 minutes and then drops again to less than $T \sim 10^5\ K$ while the expansion occurs.

Fig.5c shows the evolution of the total energy in the entire computational box over the simulation. There is a slight increase of the total over the simulation due to the fact that the simulation does not take place in an isolated box. The lower boundary conditions are fixed and as a result of the magnetic field in the ghost cells not being in equilibrium a Poynting flux (thus energy) is injected into the simulation box. Moreover, mass, energy, and magnetic flux are allowed to cross the upper boundary which leads to losses. Such phenomenon, although present, was not significant in our previous work (Pagano et al. 2013a) becasue of the different β regime where the uniform pressure distribution led to the majority of energy being stored as internal energy.

Throught the simulation the majority of the total energy is stored in magnetic energy. Later on in the simulation, a portion of the magnetic energy is converted into internal and kinetic energy and thus the magnetic energy decreases. The internal energy increases, to about one third of the magnetic energy, but the simulation always develops in a mostly low-β regime. The kinetic energy is initially zero, but it quickly increases to be greater than the internal energy and flattens at about 35% of the total energy. The code solves the MHD energy equation (Eq.4) by computing the partial time derivative of the total energy, e. When magnetic energy is lost from one time step to another because of numerical resistivity or the same happens to kinetic energy because of numerical viscosity this energy is automatically converted into thermal energy through Eq.5.

Finally, Fig.6 shows the position of the centre of the flux rope and the top of the flux rope as a function of time. The parameters we have chosen for the simulation set conditions in which the flux rope is expelled from the low solar corona due to the high intensity of the initial Lorentz force and the low resistance of the solar corona. The flux rope undergoes an acceleration phase for the first 20 minutes and then it travels outwards at approximatelty constant speed. Whereas the average speed for the centre of the flux rope is $v \sim 419\ km/s$, the top of the flux rope, corresponding to the CME front travel faster at $v \sim 825\ km/s$ because of the combined motion of propagation and expansion.

2.2. Role of thermal conduction and radiative losses

The simulation presented here aims to reproduce a realistic temperature profile in order to synthetise the emission visible from AIA/SDO. In order to do so, unlike our previous work, we have implemented some non-ideal MHD terms in Eq.4. We now consider the conquence of these. Ther-

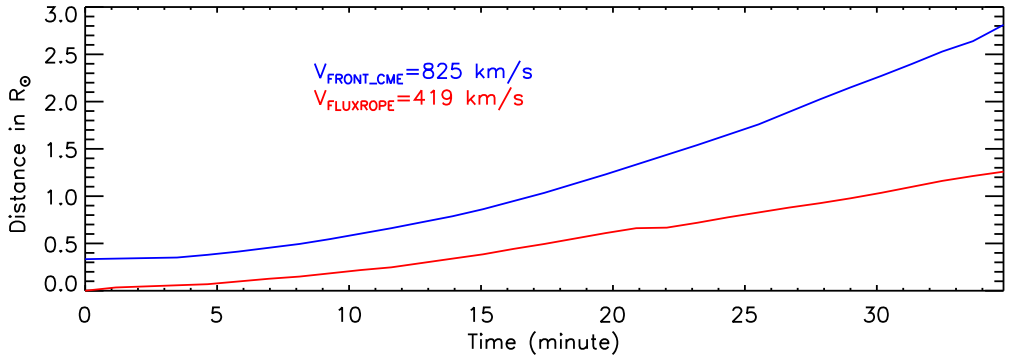

Fig. 6. Distance travelled by the centre and the top of the flux rope as a function of time.

mal conduction in the solar corona is extremely efficient along magnetic field lines and since the thermalization times are much shorter than quasistable evolution times, it plays no role during equilibrium conditions. Thus the plasma is isothermal along a magnetic field line. However, thermal conduction becomes very important for events like CMEs where plasma is rapidly heated. In our simulation, thermal conduction does not significantly affect the flux rope temperature, as the flux rope is embedded in magnetic field lines where the thermal gradient is perpendicular to the magnetic field lines. Thus any heat exchange with the surroundings is prevented. In contrast, thermal conduction does become effective at the hot front where thermal gradients are parallel to magnetic field lines and the configuration is such as to allow heat flows. The thermalization time scale in the solar corona, τ_c, in CGS unites is given by (Pagano et al. 2007):

$$\tau_c = \frac{21 n k_b L^2}{18.4 \times 10^{-7} T^{2.5}} \tag{12}$$

where L is a characteristic length scale and n is the number density. Average estimations in our simulations are $L \sim R_\odot/2$, $n \sim 10^7\ cm^{-3}$ and $T \sim 10^6.4\ K$, thus $\tau_c \sim 1000\ s$. The presence of thermal conduction allows heat flow along the magnetic field lines leading to a more uniform temperature profile along these magnetic field lines. This occurs over time scales comparable to the dynamic time scales of our MHD simulation. In contrast, radiative losses do not have a significant effect on either the hot front, nor the flux rope. The time scale of radiative losses is:

$$\tau_r = \frac{3}{2} \frac{k_b T}{n P(T)} \tag{13}$$

where $P(T)$ is the radiative losses per unit emission measure function (Raymond & Smith 1977) and can be computed as $P(T) = 10^{-17.73} T^{-2/3}$ in our temparature range (Rosner et al. 1978)). Thus, using flux rope values for the particle density n, we have $\tau_r \sim 10^4\ s$.

In order to test these considerations we run another simulation identical to the one presented in Sec.2, without the non-ideal MHD source terms in Eq.4. Fig.7a shows the temperature difference between the simulations with and without the non-ideal source terms. The temperatures between the two models are significantly different where the difference ranges about 1 MK (with peaks

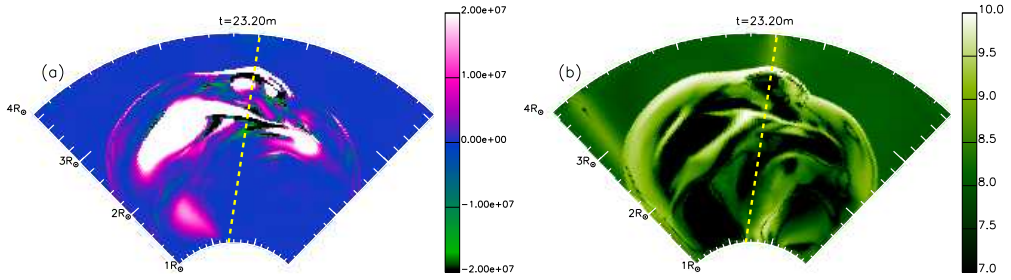

Fig. 7. (a) Map of temperature difference between the simulation where the non-ideal terms are considered and the simulation without them in the $(r-\phi)$ plane passing through the centre of the bipoles at $t = 23.20min$. (b) Map of Log_{10} of the module of temperature gradient along the magnetic field on the same plane and at the same time.

up 20 MK), higher or lower. The difference in temperature shows that an ideal MHD modelling can both overestimate or underestimate the temperatures by as much as 1 MK. It should be noted that significant differences are only evident ahead of the flux rope ejection and at the sides of the bipoles, in the front of the ejection.

In the region of the flux rope motion (along the yellow dashed cut) there is a good agreement between the two simulations within a temperature of about 2×10^4 K. This is because the highly twisted magnetic field of the flux rope prevents heat exchange and thermal condution is inefficienct there.

In Fig.7b, we show the module of temperature gradient along the magnetic field lines

$$|\nabla T_{\|B}| = |\frac{\nabla T \cdot \mathbf{B}}{|\mathbf{B}|}| \tag{14}$$

(for the simulation where non-ideal terms are considered). Visibly the region where the gradient is minimum corresponds to the center of the flux rope, while the regions that show a greater temperature difference in Fig.7a mostly correspond to regions where the quantity $|\nabla T_{\|B}|$ is higher in Fig.7b.

3. AIA Emission synthesis

We develop a simple technique that synthesizes the observations of AIA from our MHD simulation with the use of the AIA module in Solar Software. The synthesis is carried out as follows in three steps: (i) with the AIA module of the Solar Software we create the instrumental response function for each channel as function of temperature, (ii) we then compute the synthetized emission from each cell of the MHD simulation (interpolated in a 3D cartesian domain), (iii) finally we integrate along the line of sight. Therefore, we compute the emission from each element of plasma observed by each EUV channel of AIA as:

$$EM_{ch.}(n,T) = n^2 \zeta(T)_{ch.} \tag{15}$$

where $\zeta(T)_{ch.}$ is provided by the AIA module in Solar Software. Fig.8 shows the functions $\zeta(T)_{ch.}$ for all the channels from the AIA module in Solar Software. For all the channels the emission

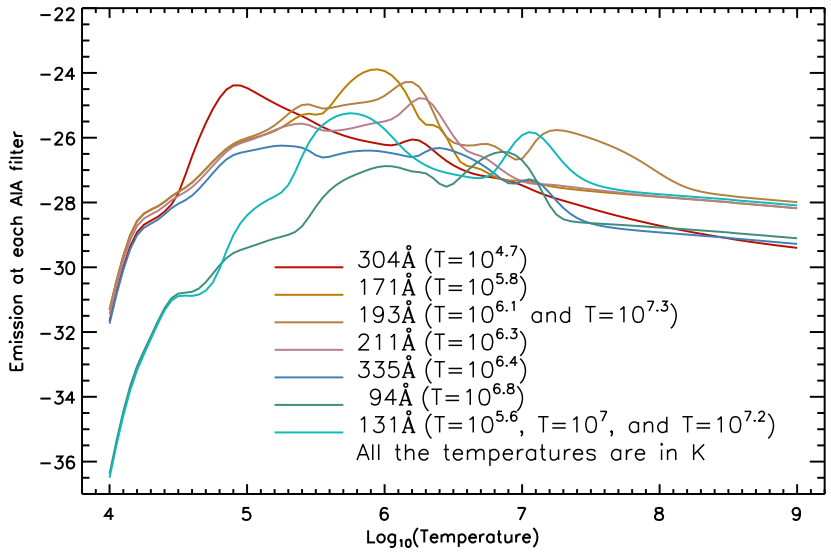

Fig. 8. Values of $Log_{10}(\zeta(n,T)_{ch.})$ for all the AIA channels as a function of T

peak lies far from our temperature extrema at $T = 10^4\ K$ and $T = 10^9\ K$. This temperature range includes the temperature values found in our simulation.

4. Results

In the present paper, we perform a MHD simulation of the ejection of a magnetic flux rope and then we apply a simple emission model to synthesize the corresponding observations of AIA. In particular, we show here the synthesized observations for 4 of the AIA channels (304Å, 171Å, 335Å and 94Å) where these channels show the evolution of the flux rope ejection in the solar corona at commonly observed temperatures. In Sec.4.1 we describe the synthesized observations from the channels at 304Å (peak at $T \sim 10^{4.7}\ K$) and 171Å (peak at $T \sim 10^{5.8}\ K$), observing relatively cool plasma. In Sec.4.2 we describe the synthesized observations from the channels at 335Å (peak at $T \sim 10^{6.4}\ K$) and 171Å (peak at $T \sim 10^{6.8}\ K$), observing hot plasma.

4.1. Cold Channels: 304Å *and* 171Å

In Fig.9 we show the synthesized observations of 304Å and 171Å channels from the simulation at $t = 0$, 11.60 and 23.20 *min* where the flux rope initially lies on the solar surface at 30° from the plane of sky in the direction of the observer. This is a point of view that has no particular symmetry, thus is suitable to describe a general ejection. The field of view used in Fig.9 is $1.5 \times 2.15\ R_\odot$ wide and represents a portion of the disk as can be viewd by AIA. Fig.9 shows the logarithm of synthetized data numbers per second.

Initially the flux rope is clearly visible in the 304Å and 171Å channels (Fig.9a). The flux rope is slightly larger in the 171Å channel, as this channel picks out the external shell of the flux rope as it is more sensitive to higher temperatures than the 304Å channel.

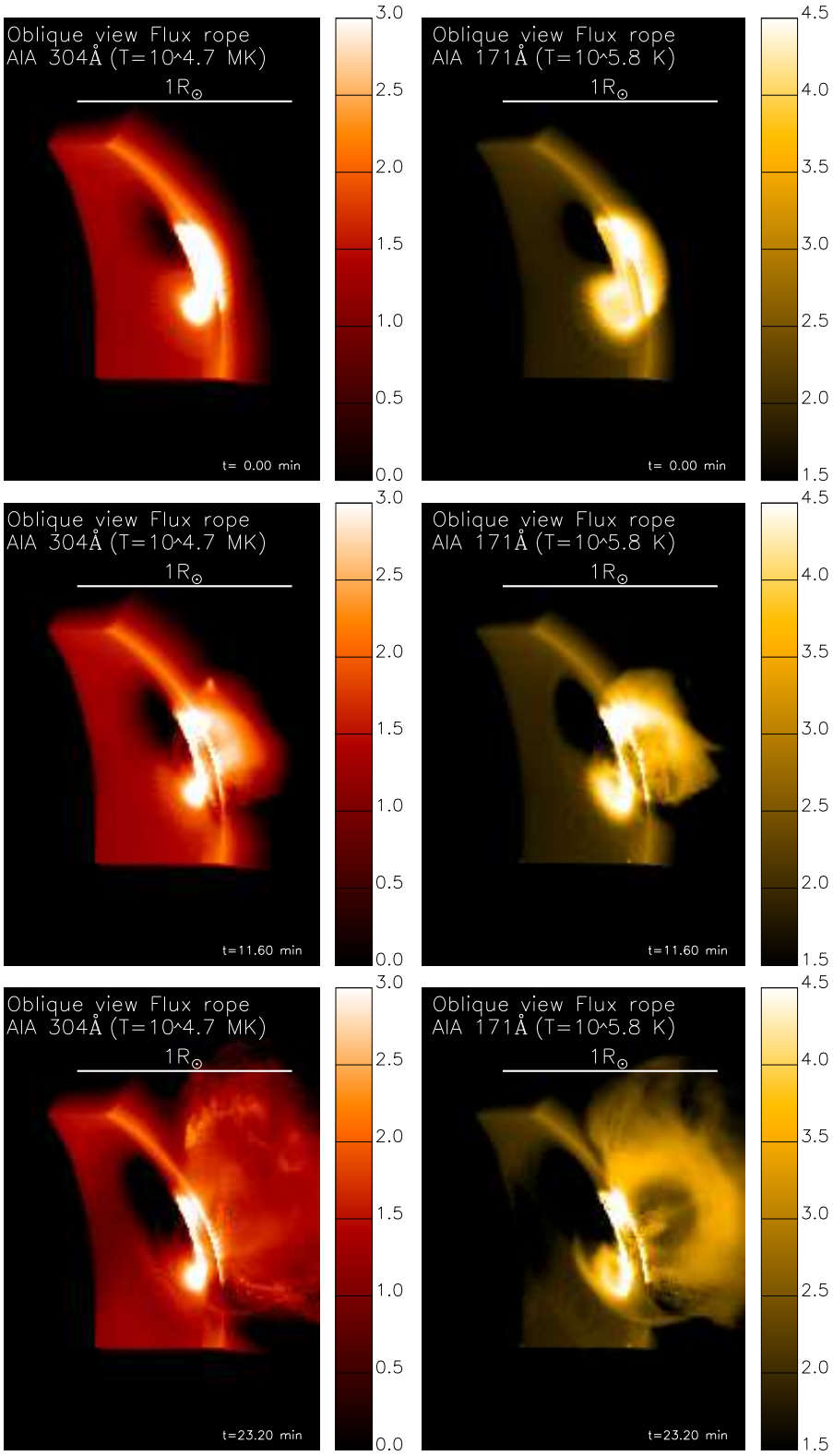

Fig. 9. Synthesized observations of AIA in the 304Å and 171Å channels at (a) $t = 0$ *min*, (b) $t = 11.20$ *min* and (c) $t = 23.20$ *min*. All maps show the logarithm of synthetized data numbers. The temporal evolution is available in the on-line edition.

At $t = 11.60$ *min* the ejection has already occurred and it presents several observable features. In both channels the eruption is clearly visible with an arc shaped structure that is moving outwards. In the 171Å channel the structure is further from the Sun because of the different temperature

sensibility. Similarly, the 171Å channel shows a small void under the arc of the ejecting flux rope which is not visible in the 304Å channel. In both channels it is possible to notice some fragmentation of the structure at its sides, and in the 171Å channel the strucuture seems to be more clearly anchored to its Northern footpoint. Comparing the position of the structures in Fig.9b and the analysis of the position of the flux rope centre carried on in Fig.6, it is possible to infer that they both correspond to the ejected flux rope, and the front is already out of the field of view. Although at $t = 11.60\ min$ the flux rope temperature is far from the $10^{4.7}\ K$ peak of the 304Å channel, the ejection is visible in this channel because of the high density of the flux rope plasma at $T = 1\ MK$, a temperature at which the 304Å still has a significant response (Fig.8). Similar but more expanded features are observed in the images at $t = 23.20\ min$ (Fig.9c). In both channels the ejected flux rope has expanded and clearly looks like a circular ejection with a void placed in the center of the ejection in the 171Å channel. The 304Å presents a non uniform emission that evidently shows how the eruption opens up, in spite of the fact that the flux rope is no longer clearly visible. The fragmentation at the edges of the ejection is very evident in both 304Å and 171Å channels, due to the strong temperature disuniformities. At the same time, it can be seen that the solar surface has been perturbed by the ejection. In all of the images shown in Fig.9, the absolute data numbers obtained in our study are comparable to within an order of magnitude with actual off-limb observations from AIA during solar eruptions.

4.2. Hot Channels: 335Å *and* 94Å

The flux rope ejection appears significantly different when observed in the 335Å and 94Å channels. Initially, the flux rope is only visible in the 335Å channel, whereas the 94Å channel only shows some brithness variation around the flux rope region, but no clear evidence of its existence (Fig.10a).

As the 335Å and 94Å channels are sensitive to temperatures hotter than those of the flux rope, the arc like erupting structure is not clearly visible during the ejection. At $t = 11.60\ min$ (Fig.10b) the channels show a circular dome where an arc is only slightly visible. A brightening in the region behind the ejected flux rope can be seen because it is heated to temperatures close to the peak temperature of the 335Å and 94Å channels. In contrast, the region surrounding the flux rope ejection has temperatures about 1 MK at this time (Fig4). It is worth noting that the region where the flux rope was originally placed lights up after the ejection in the 94Å channel, as plasma at this location is heated because of the conversion of magnetic energy into thermal energy.

As the ejection evolves (Fig.10c), at $t = 23.20\ min$ we see that the dome has expanded in both the 335Å and 94Å channels where a diffuse emission occurs over the whole region involved in the ejection, but the emission is still quite faint where the 304Å and 171Å channels show most of the ejected structures. In 335Å and 94Å channels the solar surface does not present a significant perturbation due to the ejection.

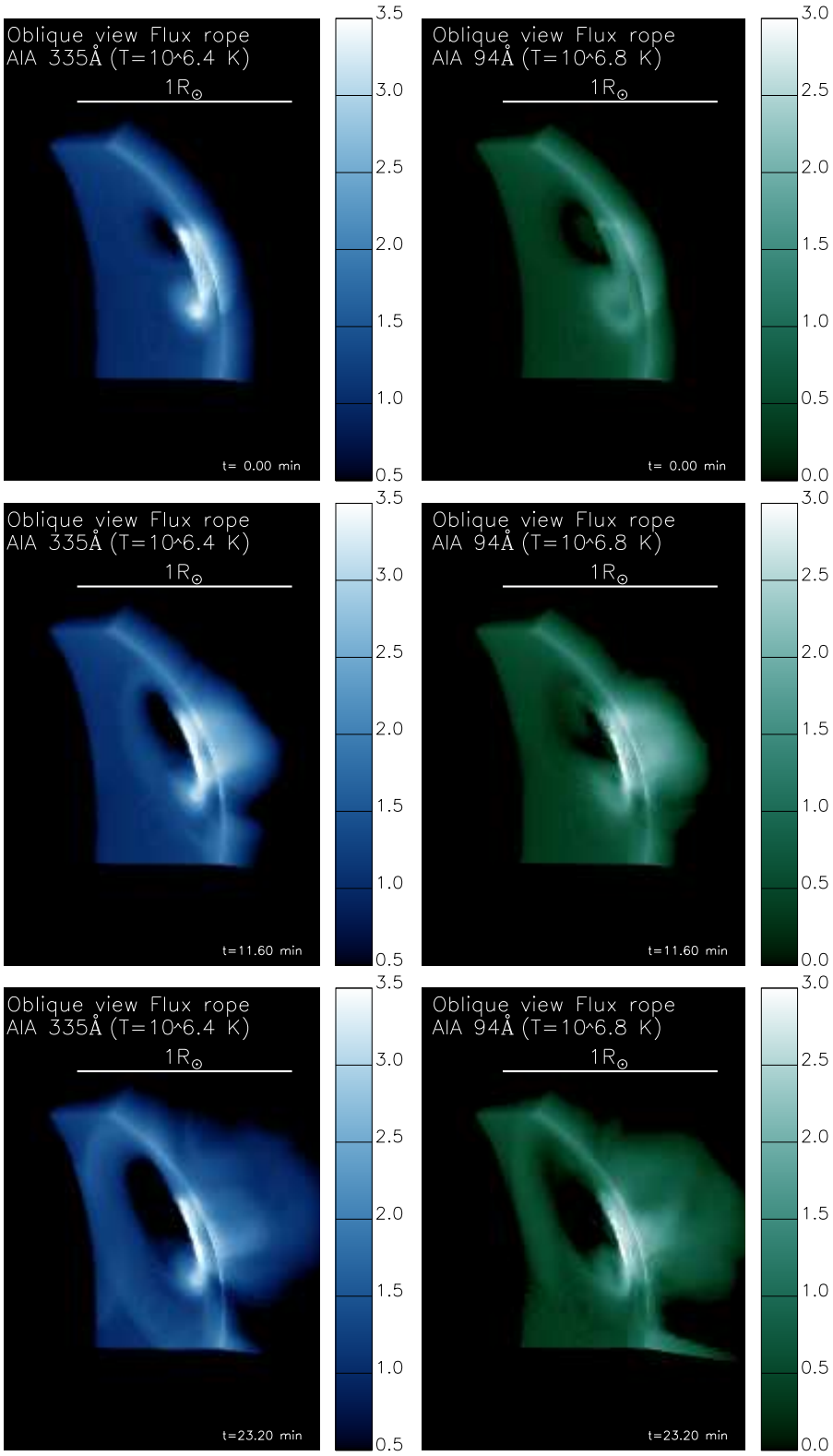

Fig. 10. Synthesized observations of AIA in the 335Å and 94Å channels at (a) $t = 0$ *min*, (b) $t = 11.20$ *min* and (c) $t = 23.20$ *min*. All maps show the logarithm of synthetized data numbers. The temporal evolution is available in the on-line edition.

5. Discussion

In the present paper we have synthesised AIA observations of a flux rope ejection. The aim of this study is to show the observational signatures of the flux rope ejection model with a simple tool that

can help verify the hypothesis upon which some models of solar eruptions are based. This enables us to understand what physical processes are behind some of the observed features of CMEs. Also, we intend to address the relevance of the effects of thermal conduction and radiative losses during flux rope ejections.

5.1. Limits and assumptions of the present work

As we aim to reproduce actual observations of the Sun, the assumptions made in our model must be carefully accounted for in order to understand the limitations of the study and so that reliable results are found and any sources of possible errors identified. Here we address the effect of the assumptions made, namely ionization equilibrium, the magnetic configuration used, and the lack of Solar Wind and transition region modelling.

The ionization equilibrium assumption is reasonable for the initial condition, but it becomes less realistic during the ejection. Pagano et al. (2008) showed that ionization equilibrium does not hold during a CME, at least for the propagating shock. However, the present work focuses especially on the ejected flux rope, where the ionization times are significantly longer than in a shock region. Fig.5 shows that the flux rope undergoes an abrupt change in temperature only in the early phase of the ejection after which the temperature slowly decreases. We thus expect Non-Ionization Equilibrium to play a marginal role for the purposes of this study. It would be important to be considered if we were to describe small scale flaring emission subsequent to the flux rope ejection initiation. This additional aspect is however beyond the scope of the present paper.

Another feature that may be important is that the initial magnetic configuration could be made more realistic, as our system is simply consisting of two bipoles and a flux rope. The actual solar corona is a much more complex environment especially during solar maximum. During maximum several CMEs per day may occur and it is possible to have multiple active regions interacting or overlapping. While this is the case, when the ejection occurs, it is normally violent enough to displace the surrounding plasma and magnetic field. Therefore the complexity around an active region should not play a major role at least in the early stages of flux rope ejections.

In order to simulate the propagation of CMEs to larger distances from the Sun we will have to include the effect of the Solar Wind. The definitive coupling between CMEs and the Solar Wind occur at 4 $R_\odot$ (Gopalswamy et al. 2000), thus it is not crucial in the spatial domain we consider, however Pomoell & Vainio (2012) explained the influence of solar wind in the thermodynamics of the plasma during ejections.

Finally, if we wish to accurately describe the emission from the solar surface in response to the ejection, we would need to include in our modelling a transition region. This is particularly important for the cold channels whose response peaks in transition region temperatures. While this is the case, as long as we focus on the off limb emission, as we do in the present work, the absence of a transition region emission should not significantly affect our conclusion.

Our work allows us to draw some similarities between the observations of CMEs seen by AIA and the observations we have synthesized here. Many of the CMEs observed with AIA present a bright arcade rising in the 304Å channel. This feature is reproduced in our work (see also the online video related to Fig.9). At the same time, in 171Å we see how the South footpoint is less ancored compared to the North one. If this phenomenon were more pronounced, leading to the complete reconnection of one footpoint with the open field, a different CME shape may be produced, like a rising tail.

In our simulation, the flux rope is clearly visible from the initial stage in the 304Å and 171Å channels. In actual AIA observations, it is common to see a bright feature from where the CME originates. While this is the case, the real magnetic configuration of the solar corona needs a more careful analysis before we can conclude the presence of a flux rope. We can however claim, though, that in both our simulation and in actual observations the ejection starts from a bright region in the 304Å channel. This tells us that to model the ejecting region with a temperature of around 10^4 K seems correct.

It should also be noted that the ejection is more evident and visible in the synthesized emission, than in the density maps we show in Fig.3. As shown in Fig.4a, the ejection of the flux rope does not lead to any local spike in density, as the flux rope density always remains comparable to the surrounding plasma density. In contrast, the displacement and expansion of the structures in the 304Å and 171Å channels are evident due to the temperature effects that sharply select the plasma we observe.

It is also worth mentioning that our system is not symmetrical due to the presence of the second bipole. Similarly, the synthesized observations do not show a symmetric shape. This has an impact on the shape of the ejection. In fact, the footpoint that remains anchored to the solar surface is the one which does not interact with the magnetic field of the second bipole, while the Southern footpoint interacts with the second bipole and with this the anchoring to the solar surface becomes weaker (this was explained in details in Pagano et al. (2013a)).

In our study, the 171Å and 304Å channels results are as the most appropriate to follow the flux rope propagation, due to the flux rope temperature. However, the two channels show some differences: the emission in the 304Å channel is more diffuse and the arcade is less sharp, while the 171Å channel presents the arcade slightly further from the solar surface. In contrast, the hot channels at 335Å and 94Å are suitable to highlight the temperature increase of the plasma during the CME. In our simulation, the heating occurs at the front of the ejection (not visible in Fig.10b), and behind the propagating flux rope where magnetic energy is converted into thermal energy which results in a diffuse emission in Fig.10b-c. This latter process is very similar to a reconnection event at the current sheet as prescribed by the standard flare model and also observed in the 131Å channel by Cheng et al. (2011) from a different point of view than that considered within this study.

Finally, it is interesting to note that our synthesized observations are directly comparable with actual ones, as the synthesized data number are close to actual counts (within an order of magnitude). This shows that density and temperature values reproduced by our MHD simulations are realistic, at least for the region of corona involved. In the channel at 304Å it is usual to observe $\sim 10-100$ DN per second for off limb flux rope ejections and ~ 1000 DN per second for bright structures on the disk. The 171Å channel usually counts about one order of magnitude larger DN per second. As far as the hot channels are concerned, observations count about $\sim 1-50$ DN per second for off limb flux rope ejections. Of course, these values may vary when studying different events, but they are in reasonable agreement with our synthesis in Fig.9 and Fig.10.

5.3. Thermal conduction and radiative losses effects

Our study also tries to shed some light on the importance of thermal conductiona and radiative losses effects when we study the ejection of a flux rope. While, there is no doubt that thermal condution, radiative losses, and ohmic heating are all physical processes actually taking place in the solar corona, the question is whether they are effective during a flux rope ejection or CME. A common consequence on the use of thermal conduction term is that it results in greater computational times. A secondary effect of this is that with the increased number of timesteps needed to span a given physical time, there are larger roundoff errors with the increase of the effect of numerical diffusion. Therefore, it is worthwhile to question whether the use of these specific non-ideal terms is useful depending on the purpose of the investigation.

In the past, Reeves et al. (2010) have already made a significative attempt to model a flux rope ejection including non-ideal MHD terms and have reported interesting findings on the energetics of the CME. In particular with regard to how the ejection is initiated in a 2D domain. Our work, instead, focuses on the propagation of the flux rope and describes the effect of thermal conduction in 3 directions. Lugaz et al. (2011) represents a key work in line with the attempt we present here (although reproducing data from EIT) and we also aim at using real magnetograms of actual ejections in the future, while the present simulation starting from an idealized case allowed a thorough understanding and the synthetis of AIA images.

In the study presented here, the non-ideal MHD terms play no role in the initiation of the eruption. The eruption happens because of an unbalanced upward directed Lorentz force and, as explained in Pagano et al. (2013a), the magnetic reconnection occuring behind the ejecting flux rope is a consequence of the flux ropes motion and it only reinforces the eruption, but it is not the main cause.

As the ejection proceeds, thermal conduction and radiative losses are effective where heat flows along magnetic field lines and the plasma radiates energy. However, as shown in Fig.7 the effect of these terms in not dominant in the region of the ejection. Whether we include or do not include non-ideal MHD terms, the speed of the top and the center of the flux rope (as in Fig.6) differs by only 3 km/s. From this point of view, it seems that the dynamics of the ejection are not affected

by the thermal conduction and radiative losses terms and the consequences of heat flows and radiative losses are not fast and strong enough to affect the density, momentum and magnetic field distribution which are primarly responsible for the dynamics of the ejection.

However, as we show in Fig.7, thermal conduction does have a significant impact on the temperature distribution. Due to these effects there are differences of several MKs which cannot be neglected. The plasma temperature is a parameter of crucial importance in the solar corona for many reasons. All the small scale mechanisms (particle acceleration, plasma heating) are dependent on the temperature of plasma and they are often an important diagnostic tools to assess energetics and properties of large scale events, such as solar eruptions and solar flares.

6. Conclusions

In the present work, we synthesize EUV AIA observations of a flux rope ejection. To do so we first perform a MHD simulation where a flux rope is ejected as a consequence of it being initially out of equilibrium. We then apply a simple model of EUV emission to compute the emission from each plasma element in our simulation. We finally take into account the response to the emission of each AIA channel and integrate along the line of sight to obtain the synthesized observations. Our work is a first step in this direction, but some issues can be improved in order to have a better match between observations and models.

We will extend our coupling technique between the GNLFFF model and the MHD simulation to include the use of real magnetograms representing the full Sun as an initial condition in our MHD simulations (such as used in Yeates et al. (2010)). This will reproduce more complex and realistic patterns of the solar corona that result in flux rope ejections. We will also focus on modelling specific events using idealized initial magnetic configurations inspired by observed magnetic structures prior to ejections. Even though the above improvements are required, the current status of the modelling technique is sufficient to reproduce many of the main features presently found in observations.

Another aspect of the work presented here is that we are not restricted to constructing synthetic AIA observations. The same technique may be applied to the EUV channels observed by the EUI instrument on board Solar Orbiter. Thus the development of this technique provides a platform for the prediction of features that may be observed by Solar Orbiter.

Acknowledgements. DHM would like to thank STFC, the Leverhulme Trust and the European Commission's Seventh Framework Programme (FP7/2007-2013) for their financial support. PP would like to thank the European Commission's Seventh Framework Programme (FP7/2007-2013) under grant agreement SWIFF (project 263340, www.swiff.eu) for financial support. These results were obtained in the framework of the projects GOA/2009-009 (KU Leuven), G.0729.11 (FWO-Vlaanderen) and C 90347 (ESA Prodex 9). The research leading to these results has also received funding from the European Commission's Seventh Framework Programme (FP7/2007-2013) under the grant agreements SOLSPANET (project n 269299, www.solspanet.eu), SPACECAST (project n 262468, fp7-spacecast.eu), eHeroes (project n 284461, www.eheroes.eu). The computational work for this paper was carried out on the joint STFC and SFC (SRIF) funded cluster at the University of St Andrews (Scotland, UK). CHIANTI is a collaborative project involving George Mason University, the University of Michigan (USA) and the University of Cambridge (UK).

References

Amari, T., Aly, J.-J., Luciani, J.-F., Mikic, Z., & Linker, J. 2011, ApJ, 742, L27

Amari, T., Luciani, J. F., Aly, J. J., Mikic, Z., & Linker, J. 2003, ApJ, 585, 1073

Amari, T., Luciani, J. F., Mikic, Z., & Linker, J. 2000, ApJ, 529, L49

Archontis, V., Hood, A. W., Savcheva, A., Golub, L., & Deluca, E. 2009, ApJ, 691, 1276

Aulanier, G., Török, T., Démoulin, P., & DeLuca, E. E. 2010, ApJ, 708, 314

Chen, P. F. 2011, Living Reviews in Solar Physics, 8, 1

Cheng, X., Zhang, J., Liu, Y., & Ding, M. D. 2011, ApJ, 732, L25

Colgan, J., Abdallah, Jr., J., Sherrill, M. E., et al. 2008, ApJ, 689, 585

Dere, K. P., Landi, E., Mason, H. E., Monsignori Fossi, B. C., & Young, P. R. 1997, A&AS, 125, 149

Downs, C., Roussev, I. I., van der Holst, B., et al. 2011, ApJ, 728, 2

Fan, Y. 2009, ApJ, 697, 1529

Fan, Y. 2010, ApJ, 719, 728

Fan, Y. & Gibson, S. E. 2007, ApJ, 668, 1232

Forbes, T. G. & Isenberg, P. A. 1991, ApJ, 373, 294

Gopalswamy, N., Lara, A., Lepping, R. P., et al. 2000, Geophys. Res. Lett., 27, 145

Hoilijoki, S., Pomoell, J., Vainio, R., Palmroth, M., & Koskinen, H. E. J. 2013, Sol. Phys., 286, 493

Keppens, R., Meliani, Z., van Marle, A. J., et al. 2012, Journal of Computational Physics, 231, 718

Landi, E., Young, P. R., Dere, K. P., Del Zanna, G., & Mason, H. E. 2013, ApJ, 763, 86

Lemen, J. R., Title, A. M., Akin, D. J., et al. 2012, Sol. Phys., 275, 17

Li, L. P. & Zhang, J. 2013, A&A, 552, L11

Lionello, R., Linker, J. A., & Mikić, Z. 2009, ApJ, 690, 902

Lugaz, N., Downs, C., Shibata, K., et al. 2011, ApJ, 738, 127

Mackay, D. H. & van Ballegooijen, A. A. 2006, ApJ, 641, 577

Mok, Y., Mikić, Z., Lionello, R., & Linker, J. A. 2005, ApJ, 621, 1098

Pagano, P., Mackay, D. H., & Poedts, S. 2013a, A&A, 554, A77

Pagano, P., Mackay, D. H., & Poedts, S. 2013b, A&A, 554

Pagano, P., Raymond, J. C., Reale, F., & Orlando, S. 2008, A&A, 481, 835

Pagano, P., Reale, F., Orlando, S., & Peres, G. 2007, A&A, 464, 753

Pomoell, J. & Vainio, R. 2012, ApJ, 745, 151

Powell, K. G., Roe, P. L., Linde, T. J., Gombosi, T. I., & de Zeeuw, D. L. 1999, Journal of Computational Physics, 154, 284

Raymond, J. C. & Smith, B. W. 1977, ApJS, 35, 419

Reeves, K. K., Linker, J. A., Mikić, Z., & Forbes, T. G. 2010, ApJ, 721, 1547

Rosner, R., Tucker, W. H., & Vaiana, G. S. 1978, ApJ, 220, 643

Roussev, I. I., Galsgaard, K., Downs, C., et al. 2012, Nature Physics, 8, 845

Savcheva, A., Pariat, E., van Ballegooijen, A., Aulanier, G., & DeLuca, E. 2012, ApJ, 750, 15

Spitzer, L. 1962, Physics of Fully Ionized Gases (Physics of Fully Ionized Gases, New York: Interscience (2nd edition), 1962)

Török, T. & Kliem, B. 2007, Astronomische Nachrichten, 328, 743

Tousey, R. 1973, in Space Research, ed. M. J. Rycroft & S. K. Runcorn, 713–+

Vourlidas, A., Lynch, B. J., Howard, R. A., & Li, Y. 2013, Sol. Phys., 284, 179

Yeates, A. R., Attrill, G. D. R., Nandy, D., et al. 2010, ApJ, 709, 1238

Zuccarello, F. P., Meliani, Z., & Poedts, S. 2012, ApJ, 758, 117

List of Objects